

## Decay of nonlinear whistler mode waves: 1D versus 2D

Takayuki Umeda, Shinji Saito, and Yasuhiro Nariyuki

Citation: [Physics of Plasmas](#) **25**, 072118 (2018); doi: 10.1063/1.5031483

View online: <https://doi.org/10.1063/1.5031483>

View Table of Contents: <http://aip.scitation.org/toc/php/25/7>

Published by the [American Institute of Physics](#)

---

### Articles you may be interested in

[Parametric decay of oblique whistler waves in the Earth's magnetosphere: 2-D PIC simulations](#)  
[Physics of Plasmas](#) **25**, 072901 (2018); 10.1063/1.5037763

[Laboratory space physics: Investigating the physics of space plasmas in the laboratory](#)  
[Physics of Plasmas](#) **25**, 055501 (2018); 10.1063/1.5025421

[A new method for analyzing and visualizing plasma simulations using a phase-space tessellation](#)  
[Physics of Plasmas](#) **25**, 072109 (2018); 10.1063/1.5037348

[Nonlinear evolutions of large amplitude oblique whistler waves](#)  
[Physics of Plasmas](#) **25**, 062904 (2018); 10.1063/1.5011775

[Scattering by the broadband electrostatic turbulence in the space plasma](#)  
[Physics of Plasmas](#) **25**, 072903 (2018); 10.1063/1.5039687

[Whistler modes in highly nonuniform magnetic fields. I. Propagation in two-dimensions](#)  
[Physics of Plasmas](#) **25**, 082108 (2018); 10.1063/1.5030703

---

## Decay of nonlinear whistler mode waves: 1D versus 2D

Takayuki Umeda,<sup>1(a)</sup> Shinji Saito,<sup>1,2</sup> and Yasuhiro Nariyuki<sup>3</sup>

<sup>1</sup>*Institute for Space-Earth Environmental Research, Nagoya University, Nagoya 464-8601, Japan*

<sup>2</sup>*Graduate School of Science, Nagoya University, Nagoya 464-8602, Japan*

<sup>3</sup>*Faculty of Human Development, University of Toyama, Toyama 930-8555, Japan*

(Received 30 March 2018; accepted 29 June 2018; published online 19 July 2018)

Direct comparison between one-dimensional (1D) and two-dimensional (2D) models for the development of a nonlinear, short-wavelength, and monochromatic electromagnetic whistler mode wave is made by means of fully electromagnetic particle-in-cell simulations. The 1D and 2D simulations are performed for low beta conditions in which the plasma pressure is much lower than the magnetic pressure, although the plasma kinetic energy in the direction perpendicular to the ambient magnetic field is highly dominant due to the velocity field of the imposed parent whistler mode wave. A three-wave parametric decay of the parent whistler mode wave was reconfirmed in the 1D simulation. On the other hand, a rapid decay of the parent whistler mode wave thorough a five-wave interaction or double three-wave interactions was seen in the 2D simulation. Electron heating processes in the 2D simulation are also different from those in the 1D simulation. It is suggested that the present 2D decay process is a new instability which is quite different from velocity space instabilities driven by temperature/energy anisotropy. *Published by AIP Publishing.*

<https://doi.org/10.1063/1.5031483>

### I. INTRODUCTION

Large-amplitude waves in plasmas are sometimes referred as “nonlinear” plasma waves. It has been known that the nonlinear plasma waves decay via various kinds of instabilities. The parametric instability is one of well-known decay processes for nonlinear and monochromatic waves, in which forward-propagating parent wave ( $P_0$ ) decays into two daughter waves ( $D_1$  and  $D_2$ ), i.e.,  $P_0 \rightarrow D_1 + D_2$ . Decay of nonlinear and monochromatic waves via parametric instabilities of various nonlinear plasma waves, such as high-frequency (right-handed-polarized) whistler mode waves,<sup>1,2</sup> circularly polarized Alfvén waves,<sup>3,4</sup> Langmuir waves,<sup>5,6</sup> and high-frequency (light mode) radio waves,<sup>7</sup> was studied in a one-dimensional (1D) spatial system.

The parametric decay of a finite-amplitude ( $\delta B^2 \sim 0.1B_0^2$ ) and monochromatic whistler mode wave with a frequency close to the electron cyclotron frequency  $\omega_{ce}$  has been (re)confirmed by our previous 1D particle-in-cell (PIC) simulation study.<sup>2</sup> In the previous study, a forward-propagating wave corresponded to the ion acoustic wave with a frequency  $\omega_1 \ll \omega_0$  and a wavenumber  $k_1 \sim 2k_0$ . A backward-propagating daughter wave was excited at a wavenumber close to that of the parent wave ( $k_2 \sim -k_0$ ) and a frequency close to that of the parent wave ( $\omega_2 \sim \omega_0$ ). Hence, the three-wave coupling condition ( $\omega_0, k_0 \Rightarrow (\omega_1, k_1) + (\omega_2, k_2)$ ) was satisfied. This decay process took place on a timescale of several hundred electron gyroperiods.

In the previous two-dimensional (2D) simulation,<sup>8</sup> on the other hand, a finite-amplitude and monochromatic whistler mode wave with the same frequency and wavenumber as in the previous 1D simulation showed a rapid decay on a timescale of 10–100 electron gyroperiods. This decay

process in 2D was different from both of the parametric decay in 1D<sup>2</sup> and decay processes of ion-scale whistler mode waves in 2D.<sup>9,10</sup>

In the present study, we make a direct comparison between the 1D and 2D simulation results on the decay of a nonlinear and monochromatic whistler mode wave with a short wavelength. Differences of the development of the decay processes, the associating energy conversion and electron heating processes between the 1D and 2D simulations are discussed.

### II. SIMULATION SETUP

We use 1D and 2D fully relativistic PIC codes in the present study. A higher-order interpolation<sup>11</sup> is combined to the charge conservation scheme<sup>12</sup> to reduce numerical noises and to improve the energy conservation.

The initial condition is identical to our previous simulation studies.<sup>2,8</sup> A one-dimensional, monochromatic, and right-hand-polarized electromagnetic plasma wave mode with a frequency close to the electron cyclotron frequency is imposed as a function only of  $x$  in 1D periodic and 2D doubly periodic systems

$$B_y[x, t] = \delta B \sin [k_{x0}x - \omega_0 t + \phi], \quad (1a)$$

$$B_z[x, t] = \delta B \cos [k_{x0}x - \omega_0 t + \phi], \quad (1b)$$

$$E_y[x, t] = \frac{\omega_0}{k_{x0}} \delta B \cos [k_{x0}x - \omega_0 t + \phi], \quad (1c)$$

$$E_z[x, t] = -\frac{\omega_0}{k_{x0}} \delta B \sin [k_{x0}x - \omega_0 t + \phi], \quad (1d)$$

with  $t = 0$  and  $\phi$  being a random phase ( $\phi = 0$  is chosen in the present study). An ambient magnetic field with an amplitude of

<sup>a)</sup>Email: taka.umed@nagoya-u.jp

$B_0$  is taken in the  $x$  direction. The applied electromagnetic fluctuations shown in Eq. (1) satisfy one of the Maxwell equations

$$\frac{\partial \mathbf{B}}{\partial t} = -\nabla \times \mathbf{E}. \quad (2)$$

To satisfy the other equation

$$\frac{1}{c^2} \frac{\partial \mathbf{E}}{\partial t} = \nabla \times \mathbf{B} - \mu_0 \mathbf{J}, \quad (3)$$

we need an electric current.

In the present study, the electric current is assumed to be supported by electrons only, i.e.,  $\mathbf{J} \sim \mathbf{J}_e = -eN_e\mathbf{U}_e$ . The electron bulk velocity (i.e., electron velocity fields)  $\mathbf{U}_e$  is obtained as

$$U_{x,e}[x, t] = 0, \quad (4a)$$

$$U_{y,e}[x, t] = \frac{k_{x0}^2 c^2 - \omega_0^2}{\omega_{pe}^2} \frac{\omega_{ce}}{k_{x0} B_0} \delta B \sin[k_{x0}x - \omega_0 t + \phi], \quad (4b)$$

$$U_{z,e}[x, t] = \frac{k_{x0}^2 c^2 - \omega_0^2}{\omega_{pe}^2} \frac{\omega_{ce}}{k_{x0} B_0} \delta B \cos[k_{x0}x - \omega_0 t + \phi], \quad (4c)$$

where  $\omega_{pe} = \sqrt{e^2 N_0 / \epsilon_0 m_e}$  and  $\omega_{ce} = -eB_0 / m_e$  are the electron plasma and cyclotron frequencies, respectively. Note that  $\omega_{ce} < 0$  for right-hand polarized waves. We also assume that both of ions and electrons have an isotropic shifted Maxwellian momentum distribution at the initial state ( $t=0$ )

$$f_{e(i)}[x, \mathbf{p}] = \frac{N_0}{(\sqrt{2\pi}V_{te(i)})^3} \exp\left[-\frac{|\mathbf{p} - m_{e(i)}\mathbf{U}_{e(i)}[x]|^2}{2m_{e(i)}^2 V_{te(i)}^2}\right], \quad (5)$$

where  $V_{te(i)} = \sqrt{T_{e(i)} / m_{e(i)}}$  represents the electron (ion) thermal velocity. The bulk velocity of ions at the initial state is set to  $\mathbf{U}_i[x] = 0$ .

Equation (4) with  $t=0$  requires both the wavenumber  $k_{x0}$  and the frequency  $\omega_0$  of the parent whistler mode for initializing the simulation. We use an analytic linear dispersion

equation for electromagnetic whistler mode waves in cold plasma with correction of finite electron beta based on the full kinetic linear dispersion equation<sup>13</sup> to obtain the frequency  $\omega_0$  of the parent whistler mode

$$\omega_0 = |\omega_{ce}| \frac{|\mathbf{k}_0| k_{x0} c^2}{\omega_{pe}^2 + \left(1 + \sqrt{\beta_e}\right) |\mathbf{k}_0|^2 c^2}, \quad (6)$$

where  $\beta_{e(i)} = 2\omega_{pe(i)}^2 V_{te(i)}^2 / \omega_{ce(i)}^2 c^2 = 2\mu_0 N_{e(i)} T_{e(i)} / B_0^2$  is the ratio of the electron (ion) plasma thermal pressure to the magnetic pressure (so-called plasma beta). The ratio of the electron plasma frequency to the electron cyclotron frequency is set as  $\omega_{ce} / \omega_{pe} = -0.2236$ , which corresponds to the initial electron beta of  $\beta_{e0} = 0.004$ .

The wavenumber of the parent whistler mode is  $k_{x0} d_e = 3.927$  (which corresponds to Mode 32 in the  $x$  direction) and  $k_{y0} = 0$ . The frequency of the parent wave is given from Eq. (6) as  $\omega_0 = 0.8865 \omega_{ce} (= -0.1982 \omega_{pe})$ . Hence, the parent wave is on the branch of a high-frequency part of electromagnetic whistler mode waves. The amplitude of the parent wave is  $\delta B^2 = 0.1 B_0^2$ , which gives an amplitude of the electron bulk velocity (velocity field) as  $|\mathbf{U}_e| \sim 0.2635c$ .

The real mass ratio  $m_i / m_e = 1836$  is used and the equal temperature  $T_i = T_e = T_0$  is assumed. The grid spacing, the time step, and the speed of light are set as  $\Delta x (= \Delta y) = \lambda_{De} = V_{te} / \omega_{pe}$ ,  $\omega_{pe} \Delta t = 0.005$ , and  $c = 100 V_{te}$ , respectively. The number of grid points is  $N_x = 5120$  for both 1D and 2D simulations and  $N_y = 1280$  for the 2D simulation. Hence, the system length is  $L_x = 5120 \lambda_{De} = 51.2 d_e$  for both 1D and 2D simulations and  $L_y = 1280 \lambda_{De} = 12.8 d_e$  for the 2D simulation, where  $d_e = c / \omega_{pe}$  is the electron inertial length. The number of particles per cell is 256 for each ion and electron component.

### III. SIMULATION RESULT

Figure 1 shows the temporal evolution of the magnetic field  $B_y$  component as a function of position  $x$  and time  $t$ . The results of the 1D and the 2D simulations are shown in

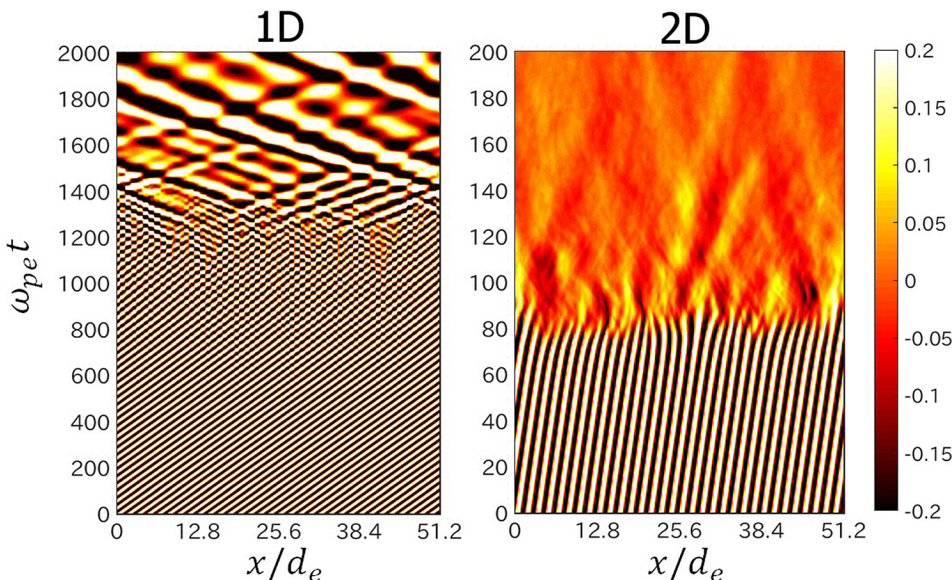


FIG. 1. Temporal evolution of the magnetic field  $B_y$  component as a function of position  $x$  and time  $t$ . The magnitude is normalized by  $B_0$ . The results of the 1D and the 2D simulations are shown in the left and the right panels, respectively. In the 2D simulation, the magnetic field at  $y=0$  is plotted.

the left and the right panels, respectively. It should be noted that there is a large difference between the timescale of 1D and 2D simulation results. Figure 1 shows the propagation of the parent wave at Mode 32 in the  $+x$  direction. The phase velocity of the parent wave ( $v_p \sim 0.05c$ ) is in good agreement with the analytical phase velocity based on the dispersion relation in Eq. (6).

In the 1D simulation, a backward-propagating wave grows from  $\omega_{pet} \sim 600$  and is visible at  $\omega_{pet} \sim 1000$  at a wavenumber  $k_{x2}d_e \sim -3.3$ . There also appears a fluctuation in the ion density at a wavenumber  $k_{x1}d_e \sim 7.2$  (not shown here). The frequency of the backward-propagating wave is estimated from the dispersion relation in Eq. (6) as  $\omega_2/|\omega_{ce}| \sim 0.87$ . The difference between the frequencies of the parent and the backward-propagating daughter wave is  $\Delta\omega/|\omega_{ce}| \sim 0.02$ , which is smaller than the ion plasma frequency  $\omega_{pi}/|\omega_{ce}| \sim 0.1$  suggesting that the fluctuation in the ion density can be on the branch of ion acoustic waves. Hence, the three-wave coupling condition is almost satisfied and the parametric decay of the parent whistler mode wave is confirmed in the 1D simulation. It should be noted that such a whistler mode wave with a short wavelength is subject to strong linear cyclotron damping if the wave amplitude is in the linear regime. However, the present parent wave exists up to  $\omega_{pet} \sim 1000$  due to its large amplitude.

At  $\omega_{pet} \sim 1300$ , wave modes propagating in both forward and backward directions are excited, which have a wavelength longer than the parent/daughter whistler mode waves. As we show later, strong electron heating takes place in the direction perpendicular to the magnetic field due to phase-space mixing of electrons between the parent and daughter whistler mode waves. Then, the electron temperature becomes anisotropic ( $T_{e\perp} > T_{e\parallel}$ ) and the temperature anisotropy instability (or well-known Weibel instability in the presence of ambient magnetic field)<sup>14</sup> is driven as a secondary instability. The wavelength becomes longer as time elapses through inverse cascade<sup>2</sup> and wave modes with a large amplitude survive at wavenumber  $k_x d_e \sim 0.5$  (Mode 4) in the 1D simulation.

In the 2D simulation, the parent wave suddenly decays at  $\omega_{pet} \sim 80$ , whose timescale is much shorter than the parametric decay in the 1D simulation. The generation of a backward daughter wave is unclear in the magnetic field  $B_y$  component. These results suggest that a 2D decay process, which does not take place in the 1D simulation, is dominant in the 2D simulation. We have performed the run up to  $\omega_{pet} = 2000$ , but no secondary instability due to the temperature anisotropy is seen in the 2D simulation (not shown here).

Figure 2 show the histories of the energy densities and the temperatures. The energy density (pressure) and the temperature are normalized by  $B_0^2/2\mu_0$  and  $T_0$ , respectively. The top panel shows the energy densities of the magnetic field ( $|B|^2 = \delta B_x^2 + B_y^2 + B_z^2$ ) and the electric field ( $|E|^2 = E_x^2 + E_y^2 + E_z^2$ ). Note that  $B_x \equiv B_0 + \delta B_x$ . In the 1D simulation, the decrease in the magnetic field energy is small because of the generation of the backward-propagating daughter wave. The increase in the magnetic field energy is seen from  $\omega_{pet} \sim 1200$  due to the secondary temperature anisotropy instability. The electric field energy is much smaller than the

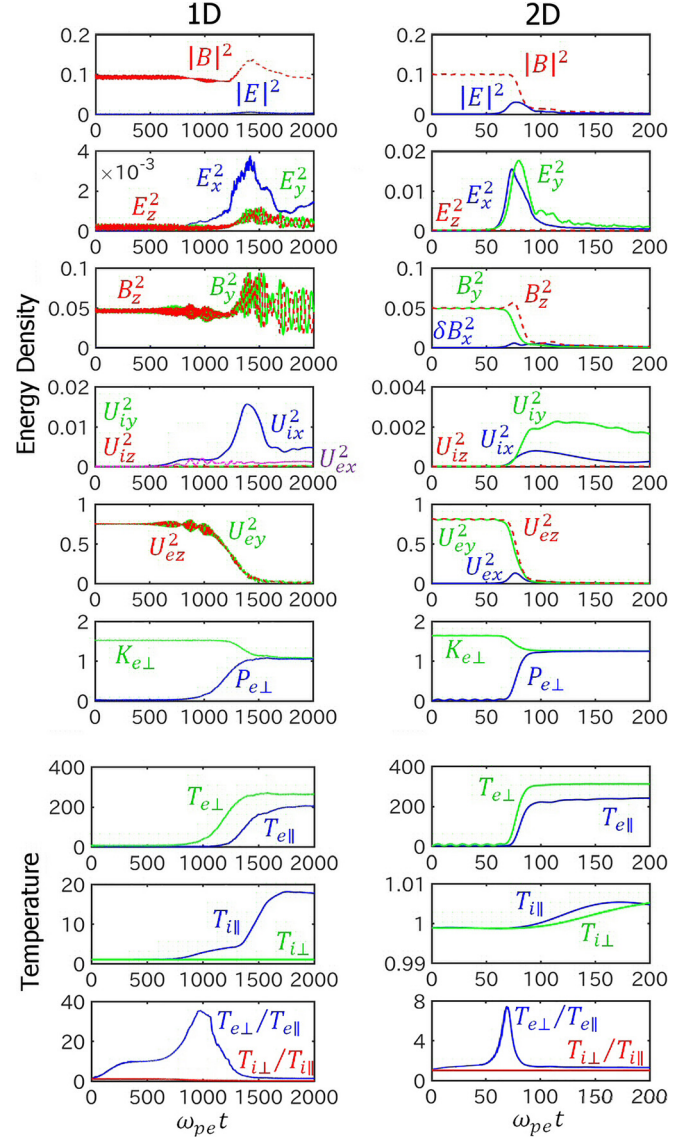


FIG. 2. Energy and temperature histories of the electromagnetic fields and particles. The results of the 1D and the 2D simulations are shown in the left and the right panels, respectively. The energy density and the temperature are normalized by  $B_0^2/2\mu_0$  and  $T_0$ , respectively.

magnetic field energy due to  $v_p \sim 0.05c$  for the parent and daughter whistler mode waves, and  $v_p \sim 0.09c$  for the whistler mode waves excited by the secondary temperature anisotropy instability. In the 2D simulation, on the other hand, the decrease in the magnetic field energy is clear. The enhancement of the electric field energy is also seen simultaneously, which implies the generation of electrostatic waves as we show later.

The second and third panels of Fig. 2 show the energy densities of each component of the electric and magnetic fields, respectively. Note that the magnetic field  $\delta B_x$  component is zero in the 1D simulation. The fourth and fifth panels show the energy densities of each component of the velocity fields for ions and electrons, respectively. (Note that the energy density of  $U_{ex}$  is plotted in the fourth panel.) In the 1D simulation, there is a small enhancement in the energy of the electric field  $E_x$  component by the parametric decay (from  $\omega_{pet} \sim 600$ ). Then, it is enhanced strongly by the

secondary temperature anisotropy instability (from  $\omega_{pe}t \sim 1200$ ). The enhancement in the energy density of the electric field  $E_x$  component has a strong correlation with the enhancement in the ion bulk energy in the direction parallel to the magnetic field ( $U_{ix}$ ) in the fourth panel. These enhancements indicate the excitation of ion acoustic waves. The enhancements in the energy densities of  $E_y$ ,  $E_z$ ,  $B_y$ , and  $B_z$  from  $\omega_{pe}t \sim 1200$  are due to bi-directional whistler mode waves excited by the secondary temperature anisotropy instability. There is an oscillation in the electron bulk energy in the direction parallel to the magnetic field ( $U_{ex}$ ) during the parametric decay at a frequency  $\omega \sim 0.025 \omega_{pe}$ , which is close to the ion plasma frequency. These results suggest that the ion acoustic waves play a role in the inverse cascade of the whistler mode waves due to the secondary temperature anisotropy instability.

In the 2D simulation, the energy densities of the electric field  $E_x$  and  $E_y$  components are enhanced during the decay of the parent wave. The magnetic field  $\delta B_x$  and  $B_z$  components are also enhanced during the decay of the parent wave, while the magnetic field  $B_y$  component shows the decrease only. There is also an enhancement in the electron bulk energy in the direction parallel to the magnetic field ( $U_{ex}$ ) during the decay of parent wave. The ion bulk energy  $U_{ix}$  and  $U_{iy}$  components are also enhanced, although they are small. As shown by our previous study,<sup>8</sup> the ion dynamics is not important in the 2D simulation.

The sixth panel shows the electron kinetic energy density and the electron pressure (i.e., thermal energy density) in the direction perpendicular to the ambient magnetic field,  $K_{e\perp}$  and  $P_{e\perp} = 2N_e T_{e\perp} = N_e (T_{ey} + T_{ez})$ . The initial perpendicular electron bulk energy ( $K_{e\perp} - P_{e\perp}$ ) due to the velocity field of the parent wave is a source of the decay instabilities. In both of the simulations, most of the electron bulk energy is converted to the perpendicular electron thermal energy during the decay of the parent wave. The final electron perpendicular temperature in the 2D simulation is slightly higher than that in the 1D simulation.

As seen in the seventh and ninth (bottom) panels, the conversion from the electron bulk energy to the perpendicular electron thermal energy generates the strong temperature anisotropy ( $T_{e\perp}/T_{e\parallel} \sim 35.5$ ) in the 1D simulation, which is a source of the secondary temperature anisotropy instability. On the other hand, the electron bulk energy is converted to both of parallel and perpendicular thermal energies of electrons in the 2D simulation. Hence, the electron temperature anisotropy in the 2D simulation is much smaller ( $T_{e\perp}/T_{e\parallel} \sim 7.4$ ) than that in the 1D simulation. Although the electron temperature anisotropy in the 2D simulation is still large, its timescale is too short for the generation of the secondary instability.

As seen in the eighth panels, there are two ion heating processes in the direction parallel to the ambient magnetic field in the 1D simulation. One takes place during the parametric decay and the other takes place during the secondary temperature anisotropy instability. The second heating process is stronger than the first one. On the other hand, the ion heating in the direction perpendicular to the ambient magnetic field is small in the 1D simulation. The ion heating is small in both directions in the 2D simulation.

The left panels of Fig. 3 show the spatial profiles of the magnetic field  $\delta B_x$ ,  $B_y$ , and  $B_z$  components, the electric field  $E_x$ ,  $E_y$ , and  $E_z$  components, the current density  $J_x$ ,  $J_y$ , and  $J_z$  components, and the charge density  $\rho$  at  $\omega_{pe}t = 75$  in the 2D simulation. The right panels show the corresponding wave-number spectra. The magnetic field, the electric field, the current density, and the charge density are normalized by  $B_0$ ,  $cB_0$ ,  $ceN_0$ , and  $eN_0$ , respectively.

Wave modes excited by the decay instability in the 2D simulation fall into three groups. The first is the sideband mode of the parent wave excited at  $(k_x, k_y) \sim (k_{x0}, \pm 1.47/d_e)$ . The sideband mode is enhanced in all of the electromagnetic components and the current density components. The excitation of multiple sidebands of this mode is also seen at  $(k_x, k_y) \sim (k_{x0}, \pm 1.47n/d_e)$ , where  $n$  is an integer number. From a Fourier analysis, we find that the frequency of this mode is close to  $\omega_0$  and that the frequency decreases as  $n$  increases (not shown here), suggesting that the sideband modes are excited on branches of oblique whistler mode waves which are linear eigenmodes. It should be noted that the frequency resolution of the Fourier analysis is low ( $\sim 0.063\omega_{pe} = 0.28|\omega_{ce}|$ ) since the decay process in the 2D simulation is fast ( $\sim 100/\omega_{pe}$ ). Hence, it is difficult to obtain the exact frequencies of the excited wave modes.

The second wave mode is a perpendicular mode excited at  $(k_x, k_y) \sim (0, \pm 1.47/d_e)$ . This mode is strongly enhanced in the  $\delta B_x$ ,  $B_z$ , and  $E_y$  components, suggesting that this mode composed of a longitudinal (i.e., electrostatic,  $\mathbf{k} \parallel \mathbf{E}$ ) component and a compressional component generated by a current filament seen in the  $J_x$  component. These components are almost steady in the timescale of  $\sim 100/\omega_{pe}$ , suggesting that the frequency of this mode is close to zero. The result means that the perpendicular mode is not on branches of linear eigenmodes. As a mechanism for the excitation of first and second modes through the decay instability in the 2D simulation, our previous study suggested a five-wave interaction of  $(\omega_0, k_{x0}, 0) \Rightarrow (\omega_0, k_{x0}, 1.47/d_e) + (\omega_0, k_{x0}, -1.47/d_e) + (0, 0, 1.47/d_e) + (0, 0, -1.47/d_e)$  or double three-wave interactions of  $(\omega_0, k_{x0}, 0) \Rightarrow (\omega_0, k_{x0}, 1.47/d_e) + (0, 0, -1.47/d_e)$  and  $(\omega_0, k_{x0}, 0) \Rightarrow (\omega_0, k_{x0}, -1.47/d_e) + (0, 0, 1.47/d_e)$ .<sup>8</sup>

The third wave mode is excited at  $(k_x, k_y) \sim (2k_{x0}, 0)$ . This mode is strongly enhanced in the  $E_x$  component only, suggesting that this mode corresponds to a longitudinal electrostatic mode. From a Fourier analysis, we find that the frequency of this mode is close to  $2\omega_0$ . It is clearly seen that this mode is enhanced in the charge density  $\rho$  but not in the current density  $J_x$  component, which indicates that this mode is excited by a nonlinear wave-wave (three-wave) coupling between the sideband whistler modes, i.e.,  $(\omega_0, k_{x0}, 1.47/d_e) + (\omega_0, k_{x0}, -1.47/d_e) \Rightarrow (2\omega_0, 2k_{x0}, 0)$ , as a secondary process. Note that this mode is also not a linear eigenmode which plays a role in a rapid electron heating as shown below.

Figure 4 shows the reduced phase-space distribution functions of electrons at different times in the 2D simulation. The four top-left panels show the  $x - v_x$  phase-space distributions obtained by integrating  $f_e(x, y, v_x, v_y, v_z)$  over  $0 \leq y/d_e \leq 0.0512$ ,  $-c \leq v_y \leq c$ , and  $-c \leq v_z \leq c$ . The four top-right panels show the  $x - v_y$  phase-space distributions obtained by

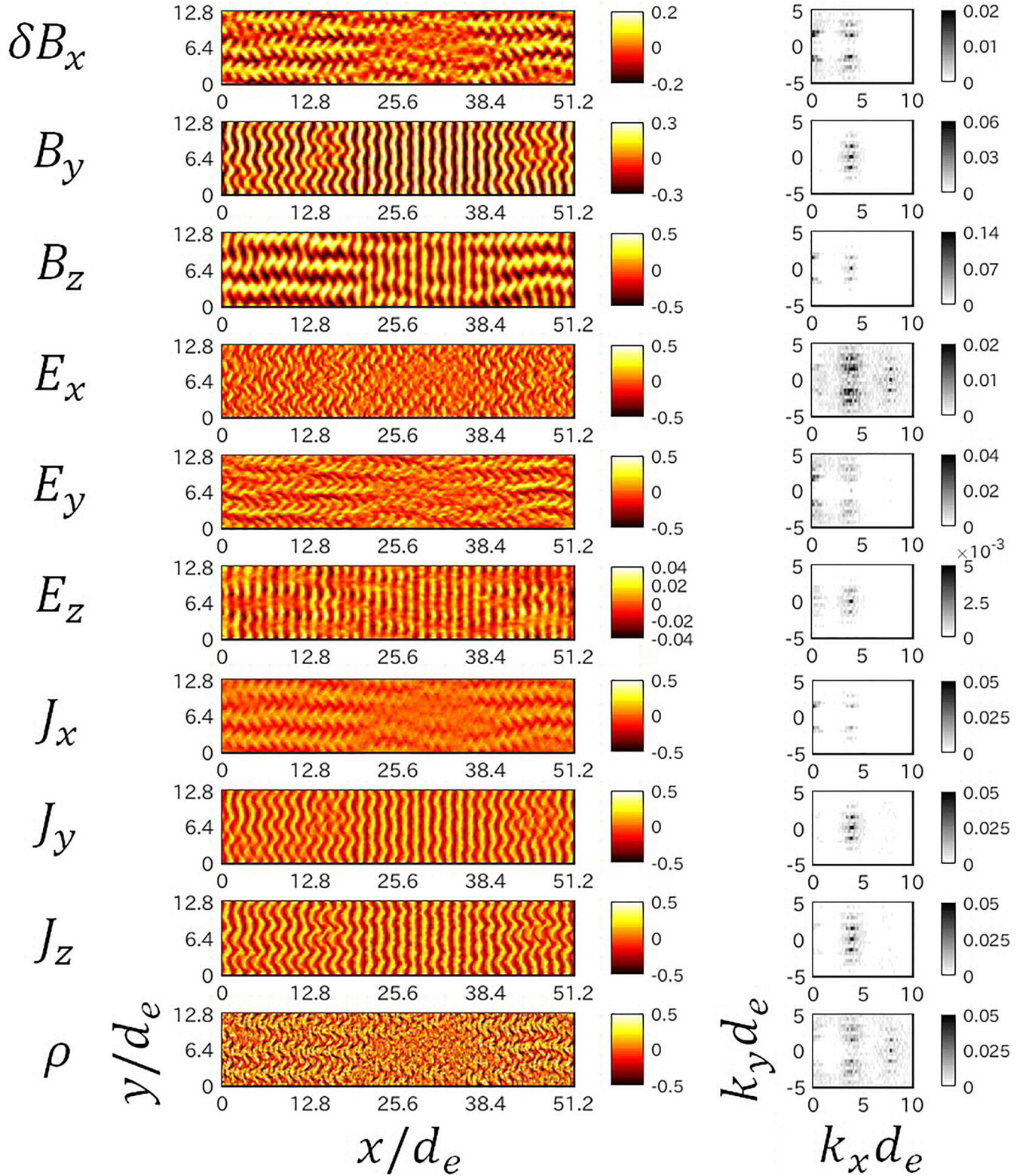


FIG. 3. Spatial profiles of the magnetic field  $\delta B_x$ ,  $B_y$ , and  $B_z$  components, the magnetic field  $E_x$ ,  $E_y$ , and  $E_z$  components, the current density  $J_x$ ,  $J_y$ , and  $J_z$  components, and the charge density  $\rho$  at  $\omega_{pe}t = 75$  in the 2D simulation (left) and the corresponding wavenumber spectra (right). The magnetic field, the electric field, the current density, and the charge density are normalized by  $B_0$ ,  $cB_0$ ,  $ceN_0$ , and  $eN_0$ , respectively.

integrating  $f_e(x, y, v_x, v_y, v_z)$  over  $0 \leq y/d_e \leq 0.0512$ ,  $-c \leq v_x \leq c$ , and  $-c \leq v_z \leq c$ . The four bottom-left panels show the  $y-v_x$  phase-space distributions obtained by integrating  $f_e(x, y, v_x, v_y, v_z)$  over  $0 \leq x/d_e \leq 0.0512$ ,  $-c \leq v_y \leq c$ , and  $-c \leq v_z \leq c$ . The four bottom-right panels show the  $y-v_y$

phase-space distributions obtained by integrating  $f_e(x, y, v_x, v_y, v_z)$  over  $0 \leq x/d_e \leq 0.0512$ ,  $-c \leq v_x \leq c$ , and  $-c \leq v_z \leq c$ .

The  $x-v_x$  phase space plots at  $\omega_{pe}t = 70$  and  $80$  show weak phase-space trapping of electrons at wavenumbers  $k_x = k_0$  by the sideband whistler modes and strong phase-space

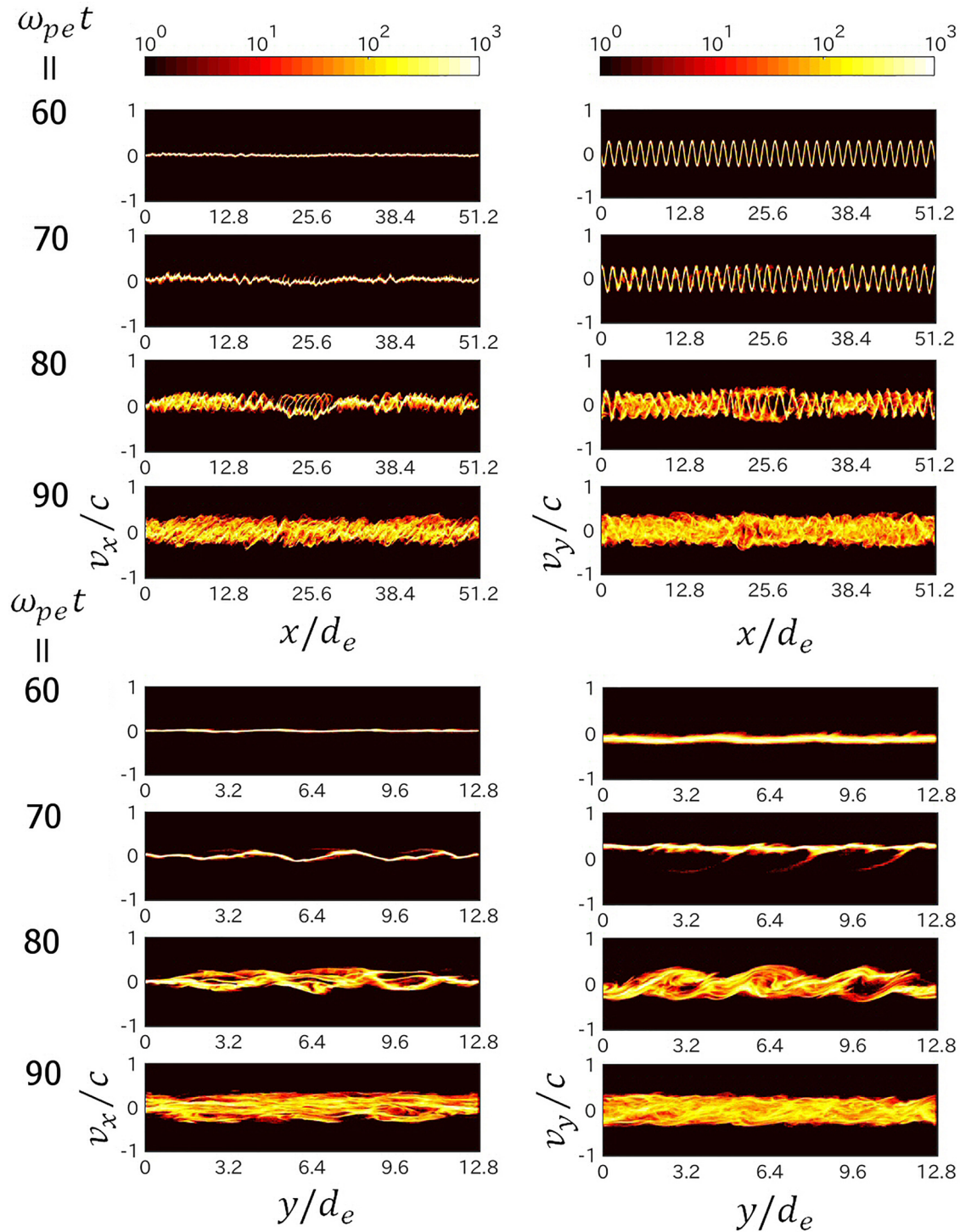


FIG. 4. Reduced phase-space distribution functions of electrons at different times in the 2D simulation.

trapping at  $k_x = 2k_0$  by the longitudinal electrostatic mode through the Landau resonance. The  $x - v_x$  phase space at  $\omega_{pet} = 80$  also indicates that no phase-space trapping is seen in the  $-x$  direction, suggesting that there is no excitation of backward wave modes and that the electron cyclotron resonance due to the forward sideband whistler mode waves is small.

The  $y - v_y$  phase space plot at  $\omega_{pet} = 70$  does not show strong electron heating (i.e., phase-space trapping) by the sideband whistler modes. On the other hand, the  $y - v_y$  phase

space plot at  $\omega_{pet} = 80$  shows phase-space trapping of electrons at wavenumber  $k_y d_e = 1.47$  (Mode 3 in the  $y$  direction), but by the transverse compressional mode. The modulation at wavenumber  $k_y d_e = 1.47$  is also seen in the  $y - v_x$  phase space plot due to the current filament.

The results show that the mechanism for the electron heating in the 2D simulation is very different from that in the 1D simulation. Electrons are heated in the direction parallel to the ambient magnetic field by strong pitch-angle scattering due to the secondary temperature anisotropy instability in

the 1D simulation, while they are heated by phase-space trapping (i.e., the Landau resonance) in the  $v_x$  space by the longitudinal electrostatic mode in the 2D simulation. Electrons are heated in the direction perpendicular to the ambient magnetic field by phase-space trapping (i.e., the cyclotron resonance) by the parent and the backward daughter waves in the 1D simulation, while they are heated by phase-space trapping in the  $v_y$  space by the transverse compressional mode ( $(k_x, k_y) \sim (0, \pm 1.47/d_e)$ ) in the 2D simulation. Hence, electrons are heated in both of the parallel and perpendicular directions by two “nonlinear” eigenmodes (i.e., longitudinal mode at  $\omega \sim 2\omega_0$  and transverse mode at  $\omega \sim 0$ ) in the 2D simulation.

**IV. COMPARISON WITH DIFFERENT INSTABILITIES**

The present decay instability in the 2D simulation, filamentary current structures is generated along the ambient magnetic field ( $J_x$  component). The formation of current filaments in an unmagnetized plasma with a temperature anisotropy has been widely known as the Weibel instability.<sup>14</sup> In

this instability, current filaments are formed in the direction parallel to the direction of the temperature anisotropy. That is, the current filaments appear in the  $J_y$  component when a temperature anisotropy exists such that  $T_y > T_{x,z}$  [e.g., Ref. 15].

Current filaments are also formed in an unmagnetized plasma with a streaming (beam) component by the Fried instability,<sup>16</sup> which is sometimes called beam-Weibel instability. In this instability, current filaments are formed in the direction parallel to the direction of the stream (i.e., in the  $y$  direction when the beam component drifts in the  $y$  direction).

The velocity distribution function in Eq. (5) corresponds to a nongyrotropic velocity distribution at each position  $x$ . With an uniform bulk velocity  $U_e = (0, |U_e|, 0)$  (here  $|U_e| = 0.2635c$ ), obliquely propagating whistler mode waves are excited but no current filament is formed.

The velocity distribution function in Eq. (5) corresponds to a ring velocity distribution when the velocity distribution is integrated over  $x$ . An uniform velocity distribution with a ring velocity  $|U_e| = 0.2635c$  in the velocity component perpendicular to the ambient magnetic field (i.e.,  $v_y - v_z$  plane) is unstable to whistler mode waves due to the same process

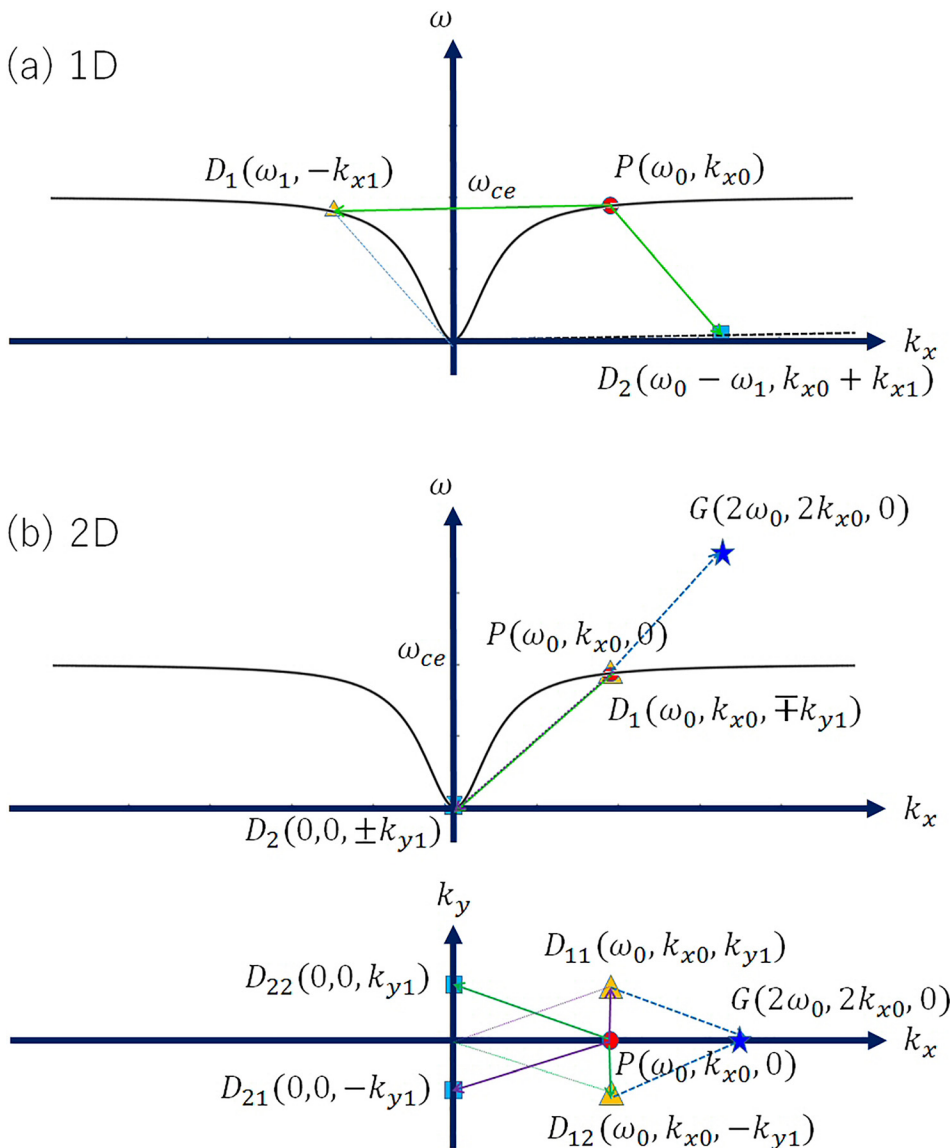


FIG. 5. Schematic illustration for the decay of a monochromatic and nonlinear whistler mode wave with a short wavelength in the 1D and 2D simulations. The circles show the parent whistler mode wave ( $P$ ). The triangles and the squares show daughter waves ( $D_1$  and  $D_2$ , respectively). The stars in 2D show a longitudinal granddaughter wave ( $G$ ) due to a secondary process.

as the temperature anisotropy.<sup>17</sup> A weak current filament is formed in the  $y$  direction (i.e., in the direction parallel to the anisotropy).

In Weibel-type anisotropy instabilities the energy/temperature anisotropy exists in the direction perpendicular to the ambient magnetic field. Then, current filaments are generated across the ambient magnetic field. In the present 2D simulation, on the other hand, current filaments develop along the ambient magnetic field, that is, in the direction perpendicular to the energy/temperature anisotropy. Also, the current filaments in the previous studies were supported by linear eigenmodes such as ion acoustic waves and lower-hybrid waves [e.g., Refs. 18 and 19]. On the other hand, filamentary current structures seen in the present study are on a branch of the nonlinear eigenmode with zero frequency. Hence, it is suggested that the 2D decay process in the present 2D simulation is a new instability for a monochromatic whistler mode wave with a large amplitude and a short wavelength.

## V. SUMMARY

A direct comparison between the 1D and 2D PIC simulations was made for the decay of a monochromatic and the nonlinear whistler mode wave with a short wavelength. A three-wave parametric decay of the parent whistler mode wave was reconfirmed in the 1D simulation. On the other hand, a rapid decay of the parent whistler mode wave through a five-wave interaction or double three-wave interactions was seen in the 2D simulation. These coupling conditions are schematically illustrated in Fig. 5. The development of the decay of the nonlinear whistler mode wave in 2D is quite different from that in 1D, because there is a channel for the excitation of waves propagating in the direction perpendicular to the ambient magnetic field in the 2D system.

It is suggested that the present 2D decay instability is a new process. In the present 2D decay instability, filamentary current structures are formed along the ambient magnetic

field, which is quite different from the development of well-known anisotropy and filamentation instabilities in which filamentary current structures are formed across the magnetic field. The filamentary current structures in the present 2D simulations are on a branch of the nonlinear eigenmode with zero frequency. Theoretical analysis of such nonlinear eigenmodes is left for a future study.

## ACKNOWLEDGMENTS

This work was supported by MEXT/JSPS under Grant-In-Aid (KAKENHI) Nos. JP26287041, JP26287119, and JP15K13572. The computer simulation was performed on the CIDAS system at the Institute for Space-Earth Environmental Research in Nagoya University through the joint research program.

<sup>1</sup>D. W. Forslund, J. M. Kindel, and E. L. Lindman, *Phys. Rev. Lett.* **29**, 249 (1972).

<sup>2</sup>T. Umeda, S. Saito, and Y. Nariyuki, *Astrophys. J.* **794**, 63 (2014).

<sup>3</sup>T. Terasawa, M. Hoshino, J.-I. Sakai, and T. Hada, *J. Geophys. Res.* **91**, 4171, <https://doi.org/10.1029/JA091iA04p04171> (1986).

<sup>4</sup>H. K. Wong and M. L. Goldstein, *J. Geophys. Res.* **91**, 5617, <https://doi.org/10.1029/JA091iA05p05617> (1986).

<sup>5</sup>I. H. Cairns, P. A. Robinson, and N. I. Smith, *J. Geophys. Res.* **103**, 287, <https://doi.org/10.1029/97JA02871> (1998).

<sup>6</sup>T. Umeda and T. Ito, *Phys. Plasmas* **15**, 084503 (2008).

<sup>7</sup>H. Usui, H. Matsumoto, and R. Gendrin, *Nonlinear Processes Geophys.* **9**, 1 (2002).

<sup>8</sup>T. Umeda, S. Saito, and Y. Nariyuki, *Phys. Plasmas* **24**, 054503 (2017).

<sup>9</sup>S. Saito, Y. Nariyuki, and T. Umeda, *Phys. Plasmas* **22**, 072105 (2015).

<sup>10</sup>S. Saito, Y. Nariyuki, and T. Umeda, *Phys. Plasmas* **24**, 072304 (2017).

<sup>11</sup>I. V. Sokolov, *Comput. Phys. Commun.* **184**, 320 (2013).

<sup>12</sup>T. Umeda, Y. Omura, T. Tominaga, and H. Matsumoto, *Comput. Phys. Commun.* **156**, 73 (2003).

<sup>13</sup>S. Saito, S. P. Gary, and Y. Narita, *Phys. Plasmas* **17**, 122316 (2010).

<sup>14</sup>E. S. Weibel, *Phys. Rev. Lett.* **2**, 83 (1959).

<sup>15</sup>C. T. Huynh and C. M. Ryu, *Phys. Plasmas* **21**, 092115 (2014).

<sup>16</sup>B. D. Fried, *Phys. Fluids* **2**, 337 (1959).

<sup>17</sup>T. Umeda, M. Ashour-Abdalla, D. Schriver, R. L. Richard, and F. V. Coroniti, *J. Geophys. Res.* **112**, A04212, <https://doi.org/10.1029/2006JA012124> (2007).

<sup>18</sup>P. Kaw, S. Schmidt, and T. Wilcox, *Phys. Fluids* **16**, 1522 (1973).

<sup>19</sup>A. F. Vinas and M. Goldstein, *J. Plasma Phys.* **46**, 129 (1991).